Nomination form for the 2021 Nishina Asia Award

Candidate (name, affiliation, curriculum vitae including the date of the degree of Ph.D., nationality, address, email and telephone)

Name

Ding ZHANG

Nationality

Chinese

Address

S705, Meng Min Wei Sci. & Technol. BLD, Tsinghua University, 100084, Haidian District, Beijing, China

Email

dingzhang@mail.tsinghua.edu.cn

Telephone

+86-010-62792385

Affiliation

Department of Physics, Tsinghua University

Employment

Dec. 2018—Present Associate Professor
Department of Physics, Tsinghua University, Beijing, China

Sep. 2016—Nov. 2018 Assistant Professor
Department of Physics, Tsinghua University, Beijing, China

May. 2014—Aug. 2016 Postdoctor
Department of Physics, Tsinghua University, Beijing, China

Education

Sep. 2008—Mar. 2014 PhD in physics
Max Planck Institute for Solid State Research, Stuttgart, Germany
Doctoral degree (summa cum laude) conferred by University of Stuttgart on March 6th, 2014
Supervisors: Dr. Jurgen Smet, Prof. Klaus von Klitzing

Sep. 2004—Jun. 2008 B.Sc. in physics
School of Physics, Peking University, Beijing, China

Honors and Awards

2020 MIT Technology Review 35 Innovators under 35 China

2020 Excellence in Advising Award, Tsinghua University

2019 Young Scholar Award, Tsinghua University

Ten Representative Publications

(1) J. Falson, Y. Xu, M. Liao, Y. Zang, K. Zhu, C. Wang, Z. Zhang, Ho. Liu, W. Duan, K. He, Ha.

Liu*, J. H. Smet*, **D. Zhang***, and Q.-K. Xue, "Type-II Ising pairing in few-layer stanene", *Science* **367**,1454 (2020), *corresponding author

(2) M. Liao, Y. Zang, Z. Guan, H. Li, Y. Gong, K. Zhu, X.-P. Hu, **D. Zhang***, Y. Xu*, Y.-Y. Wang, K. He, X.-C. Ma, S.-C. Zhang, and Q.-K. Xue*, "Superconductivity in few-layer stanene", *Nature Physics* **14**, 344 (2018), *corresponding author

(3) M. Rafique, Z. Feng, Z. Lin, X. Wei, M. Liao, **D. Zhang***, K. Jin*, and Q.-K. Xue*, "Ionic liquid gating induced protonation of electron-doped cuprate superconductors", *Nano Letters* **19**, 7775 (2019), *corresponding author

(4) M. Liao, Y. Zang, J. Zhang, R. Zhong, J. Schneeloch, G. Gu, K. Jiang **D. Zhang***, X.-C. Ma, and Q.-K. Xue*, "Superconductor-insulator transitions in exfoliated $Bi_2Sr_2CaCu_2O_{8+}x$ flakes", *Nano Letters* **18**, 5660 (2018), *corresponding author

(5) **D. Zhang***, J. Falson, S. Schmult, W. Dietsche, and J. H. Smet*, "Quasiparticle tunneling across an exciton condensate", *Physical Review Letters* 124, 246801 (2020), *corresponding author

(6) **D. Zhang**, W. Dietsche, and K. von Klitzing, "Anomalous interlayer transport of quantum Hall bilayers in the strongly Josephson-coupled regime", *Physical Review Letters* **116**, 186801 (2016), Editors' Suggestion

(7) **D. Zhang**, X. Huang, W. Dietsche, K. von Klitzing, and J. Smet, "Signatures for Wigner crystal formation in the chemical potential of a two-dimensional electron system", *Physical Review Letters* **113**, 076804 (2014)

(8) H. Zhang#, **D. Zhang#**, X. Lu#, C. Liu, G. Zhou, X.-C. Ma, L. Wang*, P. Jiang*, Q.-K. Xue, and X. Bao, "Origin of charge transfer and enhanced electron-phonon coupling in single unit-cell FeSe films on $SrTiO_3$", *Nature Communications* **8**, 214 (2017), #equal contribution

(9) **D. Zhang***, Y. Wang, N. Lu, X. Sui, Y. Xu*, P. Yu*, and Q.-K. Xue, "Origin of the anomalous Hall effect in $SrCoO_3$ thin films", *Physical Review B* **100**, 060403(R)(2019), *corresponding author

(10) **D. Zhang*#**, H. Ishizuka#, N. Lu, Y. Wang, N. Nagaosa, P. Yu* and Q.-K. Xue, "Anomalous Hall effect and spin fluctuations in ionic liquid gated $SrCoO_3$ thin films", *Physical Review B* **97**, 184433 (2018), *corresponding author, #equal contribution

Invited Talks

2019.11 Gordon Godfrey Workshop, University of New South Wales, Sydney, Australia

2019.05 Quantum Transport in 2D System-III, Luchon, France

2019.03 The American Physical Society March Meeting 2019, Boston, U.S.A.

2018.08 The 12th International Conference on Materials and Mechanism of Superconductivity and High Temperature Superconductors, Beijing, China

2017.08 International Conference on Advanced Materials, Kyoto, Japan

Citation for the Award (within 30 words)
His outstanding contributions to the discovery of Ising superconductivity in few-layer stanene
Description of the work

Stanene—a two-dimensional honeycomb lattice of tin atoms—is analogous to graphene but with promising topological properties such as the quantum spin Hall effect at room temperature and topological superconductivity, thanks to its much-enhanced spin-orbit coupling. In contrast to graphene, stanene has dangling bonds and cannot be easily exfoliated from its semi-metallic bulk counterpart—α-Sn. Researchers world-wide have since employed epitaxial methods to grow stanene and were almost exclusively focusing on revealing its topological property via studying its band-structure. In 2018, Dr. Ding Zhang and his collaborators, however, took a bold step by directly addressing the transport properties of stanene at ultralow temperatures [1]. This was, in retrospect, guaranteed by the *in-situ* passivation of stanene after growth. They found that, similar to graphene, where going from a monolayer to a bilayer makes a sharp difference, manipulating the number of atomic layers in stanene brought in profound consequences. Whereas a monolayer stanene is an insulator, superconductivity emerges in bilayer and trilayer stanene [1], raising great hope for identifying topological superconductivity in this material. Interestingly, such a delicate ultrathin film, without capping layers, was found to preserve its superconducting property for an extended period of time over one year.

If finding a new superconductor is serendipitous, uncovering its novel physical property requires scientific insight. In 2020, Dr. Zhang, leading a Sino-German collaborative team, reported yet another robust property of few-layer stanene [2]. They found that their superconductor can sustain an unexpectedly high magnetic field applied along the two-dimensional plane. Usually, Cooper pairs in a superconductor consist of spin-up and spin-down electrons such that they break up under a magnetic field that polarizes all the spins. Before the work of Dr. Zhang and his collaborators, scientists were focusing on a small group of two-dimensional materials to realize superconductors that are resilient to such a polarizing magnetic field. This so-called Ising superconductivity, in niobium diselenide for example, requires the crystal lattice to break inversion symmetry. Dr. Zhang and his collaborators found a new type of Ising pairing that utilizes the high lattice symmetry and does not require the participation of the inversion symmetry breaking. These guiding principles were soon found to be applicable to other superconductors such as palladium ditelluride. The discovery of type-II Ising pairing is a game-changer because a much-broadened material pool becomes open for exploration. Dr. Zhang made crucial contributions to this discovery not only through experimental endeavors but also by leading an international team that closely involves theoretical partners.

Apart from the representative accomplishments, Dr. Zhang has dedicated persistent efforts in addressing low-dimensional quantum phenomena, especially in high-temperature

superconductivity and quantum Hall effect. Based on his scientific achievements, Dr. Zhang well deserves the Nishina Asia Award.

Key references (up to 3 key publications*)

1. M. Liao, Y. Zang, Z. Guan, H. Li, Y. Gong, K. Zhu, X.-P. Hu, D. Zhang, Y. Xu, Y.-Y. Wang, K. He, X.-C. Ma, S.-C. Zhang, Q.-K. Xue, "Superconductivity in few-layer stanene", *Nature Physics* **14**, 344 (2018).

2. J. Falson, Y. Xu, M. Liao, Y. Zang, K. Zhu, C. Wang, Z. Zhang, Ho. Liu, W. Duan, K. He, Ha. Liu, J. H. Smet, D. Zhang, Q.-K. Xue, "Type-II Ising pairing in few-layer stanene", *Science* **367**, 1454 (2020).

*) Copy of one most significant publication should be attached.

Nominator (name, affiliation, email, telephone and relation to the candidate)

Name: Hideo Ohno

Affiliation: President, Tohoku University, Japan

Nationality: Japan

Address: 2-1-1 Katahira, Aoba-ku, Sendai, Miyagi 980-8577 Japan

Email: kenkyo-kikaku@grp.tohoku.ac.jp

Telephone: +81-22-217-5014

Signature  Date March 31, 2021

LETTERS
https://doi.org/10.1038/s41567-017-0031-6

nature physics

Superconductivity in few-layer stanene

Menghan Liao[1], Yunyi Zang[1], Zhaoyong Guan[1], Haiwei Li[1], Yan Gong[1], Kejing Zhu[1], Xiao-Peng Hu[1,2], Ding Zhang[1,2]*, Yong Xu[1,2,3]*, Ya-Yu Wang[1,2], Ke He[1,2], Xu-Cun Ma[1,2], Shou-Cheng Zhang[4] and Qi-Kun Xue[1,2]*

A single atomic slice of α-tin—stanene—has been predicted to host the quantum spin Hall effect at room temperature, offering an ideal platform to study low-dimensional and topological physics. Although recent research has focused on monolayer stanene, the quantum size effect in few-layer stanene could profoundly change material properties, but remains unexplored. By exploring the layer degree of freedom, we discover superconductivity in few-layer stanene down to a bilayer grown on PbTe, while bulk α-tin is not superconductive. Through substrate engineering, we further realize a transition from a single-band to a two-band superconductor with a doubling of the transition temperature. In situ angle-resolved photoemission spectroscopy (ARPES) together with first-principles calculations elucidate the corresponding band structure. The theory also indicates the existence of a topologically non-trivial band. Our experimental findings open up novel strategies for constructing two-dimensional topological superconductors.

Confining superconductivity to a two-dimensional (2D) plane engenders a variety of quantum phenomena[1,2]. Of late, the realization of highly crystalline and atomically thin superconductors has triggered a flurry of discoveries, including the Griffiths singularity behavior[3] and a quantum metallic phase[4,5], as well as an extremely large critical magnetic field in the plane[6,7]. One strategy for achieving 2D superconductors is to epitaxially grow superconductive single elements, such as Pb, In and Ga, for just one or two atomic layers[3,8,9]. Among the single elements, tin (Sn) is the very material in which the Meissner effect was first discovered[10], but realizing ultrathin Sn in the superconductive β-phase, known as white tin[11], remains challenging. The epitaxially grown Sn in the ultrathin limit tends to fall instead in the α-phase[12], whose bulk is semi-metallic and non-superconductive.

Recently, however, intensive research has been devoted to investigate the thinnest possible slice of α-tin(111)—a counterpart of graphene called stanene[13]. Stanene promises various exotic features, such as highly efficient thermoelectrics[14], topological superconductivity[15], and high-temperature quantum spin Hall[16] and quantum anomalous Hall effects[17]. Monolayer stanene that has been successfully fabricated by molecular beam epitaxy on Bi_2Te_3(111) (ref. [18]) and PbTe(111) (ref. [19]) is the focus of current research. On the other hand, few-layer stanene is expected to show significant thickness-dependent properties due to the strong quantum confinement[20], but its exploration is still lacking.

In this Letter, by going from monolayer to few-layer stanene, surprisingly, we discover superconductivity. We report the stable superconducting properties of uncapped few-layer stanene films on PbTe (111)/Bi_2Te_3 substrates. The superconducting transition temperature (T_c) can be effectively enhanced by varying the thickness of the PbTe buffer layer. Concomitantly with a doubling of T_c, we observe a single-band to two-band transition, which is further elucidated by photoemission spectroscopy and theoretical calculations. The calculated band structure further indicates the existence of inverted bands in our system. Our results therefore underscore the potential of an in-plane integration of 2Dtopological insulator and superconductor—of the same material. The heterostructure, vertically consisting of superconducting few-layer stanene and topological insulator Bi_2Te_3, may also be of interest for inducing topological superconductivity via the proximity effect[21].

Figure 1a schematically illustrates the sandwich structure of our system with a trilayer Sn on top of PbTe/Bi_2Te_3/Si(111). The α-phase of Sn is confirmed by in situ structural analysis (see Extended Data Figure 1). The dangling bonds on the top surface (Fig. 1a) are presumably saturated, which is evidenced by our ARPES data showing large band gaps at the K/K′ points[18,19]. The saturation might be caused by hydrogen, a ubiquitous residue in the crystal growth environment[22], resulting in chemically stable samples. Figure 1b shows that superconductivity emerges starting from a bilayer. By increasing the number of Sn layers (N_{Sn}), the transition temperature is consecutively promoted. In general, T_c scales with $1/N_{Sn}$ (Fig. 1d), as has been seen previously in other ultrathin films[1,2]. We confirm the Meissner effect by a two-coil mutual inductance technique in Extended Data Figure 2. Extended Data Figure 3 further reveals the 2D nature of such a superconductor, evidenced by anisotropic critical magnetic fields and the Berezinskii–Kosterlitz–Thouless transition. As shown in Fig. 1c, superconductivity also depends keenly on the thickness of the PbTe layer (N_{PbTe}). It emerges at $N_{PbTe}=6$, and T_c further doubles when N_{PbTe} exceeds 8. We speculate that this evolution stems from the change in density of states as well as the release of strain from the lattice mismatch (see Methods)[19]. A thicker PbTe might host more surface vacancies due to the lowered formation energy[23,24], thus providing more electron doping into Sn, as we will reveal by ARPES later. Notably, the superconductivity in these uncapped samples barely changes after exposure to air, as exemplified by the data taken in the second cool-down after more than two weeks of storage (Fig. 1c). Extended Data Figure 2 further documents the superconductivity after one year of storage. In contrast, previous ex situ transport studies on ultrathin Pb, In, and Ga films all rely on capping with an additional layer of Au or Ag[1–3]. We also show traces from two pairs of samples with the same nominal thicknesses, attesting to precise growth control. The transition temperature T_c as a function

[1]State Key Laboratory of Low-Dimensional Quantum Physics, Department of Physics, Tsinghua University, Beijing, China. [2]Collaborative Innovation Center of Quantum Matter, Beijing, China. [3]RIKEN Center for Emergent Matter Science (CEMS), Wako, Saitama, Japan. [4]Department of Physics, McCullough Building, Stanford University, Stanford, CA, USA. Menghan Liao and Yunyi Zang contributed equally to this work. *e-mail: dingzhang@mail.tsinghua.edu.cn; yongxu@mail.tsinghua.edu.cn; qkxue@mail.tsinghua.edu.cn

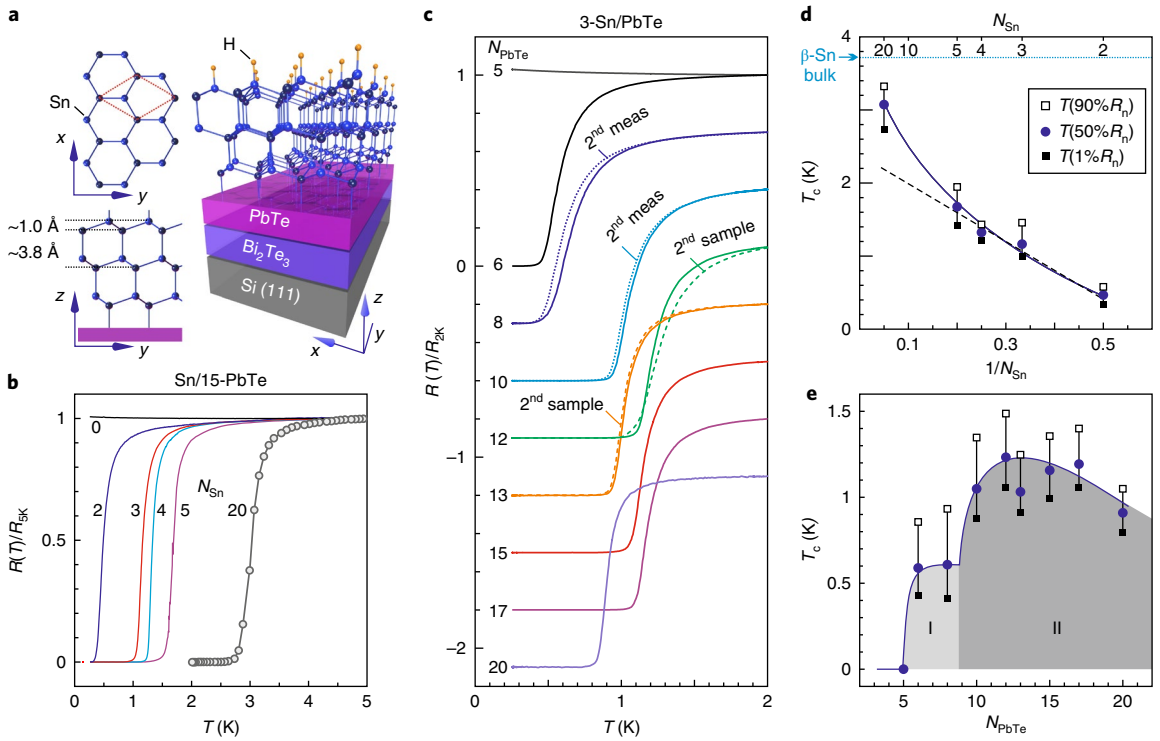

Fig. 1 | Superconductive properties of few-layer stanene. a, Illustration of stanene lattice and Sn/PbTe/Bi_2Te_3 sandwich structure. The upper left panel shows a top view of only one layer of stanene. Distances marked are from first-principles calculations. **b**, Normalized resistance of stanene with increasing number of layers grown on substrates consisting of 15-PbTe/5-Bi_2Te_3/Si(111). **c**, Normalized resistance of trilayer stanene (3-Sn) grown on different thicknesses of PbTe substrates. Numbers in the panel indicate the number of PbTe layers. Dotted curves represent the data from the second measurement after 15–20 days of storage in a glovebox. Dashed curves are from a second sample grown with the same nominal thickness. Except for the top two, the curves are equally offset for clarity. **d**,**e**, Critical temperature (T_c) as a function of the number of stanene layers (**d**) or PbTe layers (**e**). The three data points of T_c in a row represent the temperatures where the resistance drops to 1%, 50% and 90% of the normal resistance (R_n), respectively. The dashed straight line and solid curves in **d** and **e** are guides for the eye. For $N_{Sn}=20$, the superconducting transition temperature approaches that of bulk β-Sn: 3.7 K (ref. [11]).

of N_{PbTe} is given in Fig. 1e. The shaded regions represent two regimes corresponding to samples with $T_c \sim 0.5$ K and those with $T_c \sim 1.2$ K.

Transport properties of trilayer stanene in regimes I and II are distinctly different. For 3-Sn/10-PbTe in regime II, the critical current displays two steps with increasing temperature, with a kink at about 0.5 K (Fig. 2a)—a characteristic feature of two-band superconductivity[25]. This two-band nature is further confirmed by the temperature dependence of the upper critical field[26,27]. The 3-Sn/10-PbTe sample displays a concave function of $\mu_0 H_c(T)$ (Fig. 2b), which can be fitted by a formula designated for the two-band situation[26] (see Methods). In contrast to the behaviours of samples in regime II, we observe no deviation from a single-band superconductor for samples in regime I to the lowest attainable temperature. Furthermore, they show different activated behaviours in the presence of a magnetic field. For 3-Sn/8-PbTe, fittings to the activated region extrapolate to a fixed point: $1/T_c$. In contrast, 3-Sn/10-PbTe displays a continuous shift of the crossing between the adjacent extrapolated lines (dashed in Fig. 2d). The distinction is better captured by the extracted activation energy U_H and the intercept of the fitting $\ln R_0(\mu_0 H)$. In regime I, U_H scales linearly with $\ln(\mu_0 H)$, which can be described by the collective creeping of vortices[4], and the slope yields a London penetration depth Λ of 700 nm (see Methods). The Ginzburg–Landau parameter $\kappa = \Lambda/\xi$ is therefore about 23, which is much larger than $1/\sqrt{2}$, as expected for a type II superconductor. In regime II, we obtain instead a convex dependence of both U_H on $\ln(\mu_0 H)$ (Fig. 2e) and $\ln R_0$ on $U_H/k_B T_c$ (Fig. 2f). This nonlinearity may stem from field-dependent superconducting parameters of d_{sc} and Λ for multiband superconductors[28,29].

The transition from a single-band to a two-band system is corroborated by ARPES. Figure 3a displays the data of a trilayer stanene with increasing N_{PbTe}. Two valence bands can be identified: a parabolic band with its highest intensity (dark colour) below the Fermi level (E_F) and a linearly-dispersed band (white) with its two arms crossing E_F. The position of the Fermi level is distinctly different from that of bulk α-Sn (refs [30,31]). Superconductivity in few-layer stanene here may therefore stem from the enhanced density of states. By increasing N_{PbTe}, the two valence bands sink, evidenced by the decrease in energy (Fig. 3b) of the parabolic band as well as the shrinking Fermi momentum for the linear band (Fig. 3c). This indicates an increase of electron transfer from PbTe. Concomitantly, a third band becomes discernible at the Fermi level. We focus on the region just below the Fermi level in the momentum range of [−0.2, 0.2] Å^{-1}. The overall shape evolves from a rounded pyramid for 3-Sn/6-PbTe to an hour-glass structure for $N_{PbTe} \geq 10$. Such an evolution is in direct contrast to the monotonic behaviour of the residual photoelectron intensities in the gapped region, as seen in $SrTiO_3$ due to correlation effects[32]. We therefore attribute the hour-glass feature to the emergence of an electron pocket around the Γ point. In the case of 3-Sn/6-PbTe, this electron pocket may just touch the Fermi level, providing negligible contribution to transport. With further doping, the central electron pocket is significantly enlarged while the outer linear band shrinks. The trilayer stanene on PbTe with $N_{PbTe} \geq 10$ therefore behaves as a two-band superconductor. At higher doping, the enhanced interband scattering may suppress superconductivity[33], thus explaining the drop of T_c for 3-Sn on 20-PbTe (Fig. 1c,e). In addition, we estimate electron–phonon coupling constant to be 0.5 ± 0.2 for the hole band[34],

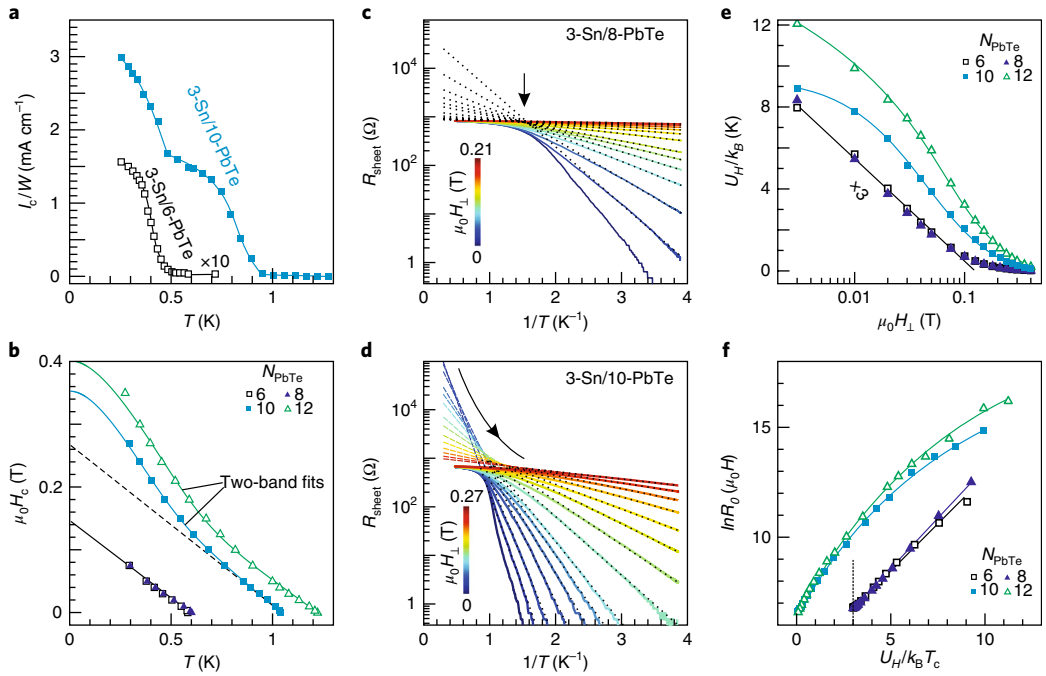

Fig. 2 | Single-band to two-band transition of a trilayer stanene. a, Critical current normalized by width of sample. Curves are guides to the eye. **b**, Upper critical field as a function of temperature. From the two-band fitting, we obtain the ratio between the diffusivities of the two bands: $D_2/D_1 \sim 0.3$. The fitting also yields the electron–phonon coupling constants for the two respective bands and the interband one: $\lambda_{11} = 0.28$, $\lambda_{22} = 0.26$, $\lambda_{12} = 0.013$ (see Methods). **c**,**d**, Arrhenius plots of the sheet resistance at different magnetic fields for two 3-Sn samples with different numbers of PbTe layers. Dotted lines are linear fits to the data in the low-temperature regime, reflecting the thermal activation behaviour. **e**, Activation energy U_H/k_B as a function of the perpendicular magnetic field. **f**, Extracted intercepts from fitting the activated transport (dotted lines in **c** and **d**). Data points for $N_{PbTe} = 6$ and 8 are horizontally offset for clarity (the dotted line marks the zero point).

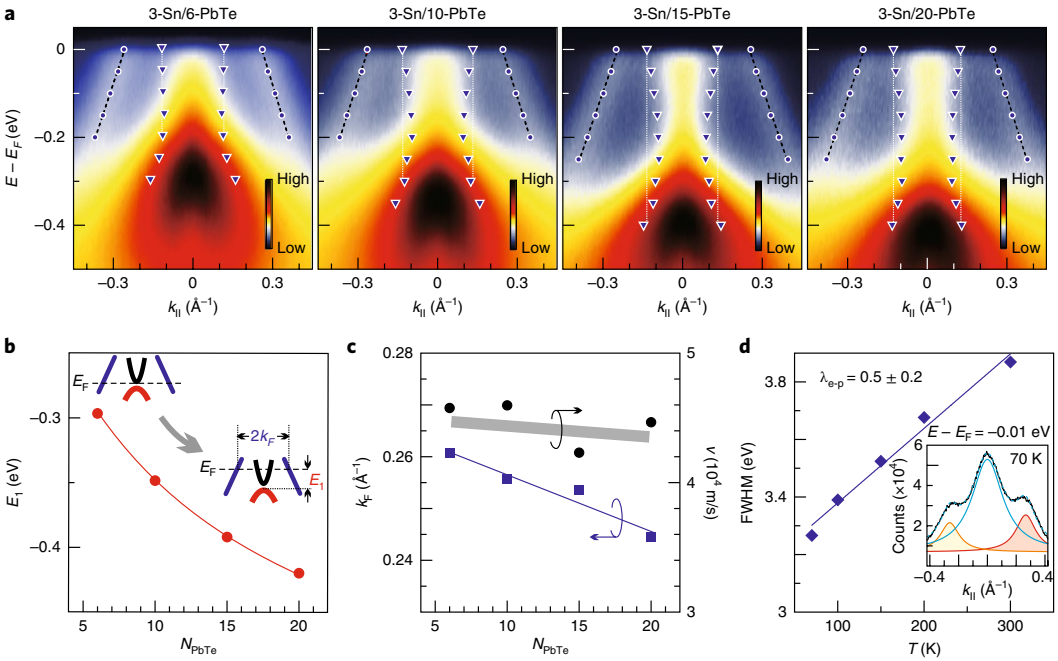

Fig. 3 | ARPES studies of a trilayer stanene. a, Band structure around the Γ point for 3-Sn grown on increasing numbers of PbTe layers. Circles mark the linear dispersion of the hole bands, with dashed lines as linear fits. Triangles demarcate the width of the central peak around $k_{||} = 0$ at different energies. Dotted vertical lines are guides to the eye. **b**, Downward shift of the energy band. The inset explains the definitions of E_1 and k_F. **c**, Fermi momentum (k_F) and the velocity of the linearly dispersed hole band as a function of N_{PbTe}. **d**, Energy width of the hole band as a function of temperature for a 3-Sn/10-PbTe sample. The electron–phonon coupling constant is estimated from a linear fitting (solid line) to the data points[34]. The estimated electron–phonon coupling constant is 0.5 ± 0.2 with the uncertainty obtained by taking into account both the Lorentzian and the linear fittings involved (see Extended Data Figure 4). The inset illustrates the Lorentzian fitting to the momentum distribution curve at $E - E_F = -0.01$ eV, 70 K. The shaded peaks reflect the hole bands. The energy width is calculated from the product of the momentum width of the shaded peaks (Δk) and the slope of the band (dE/dk).

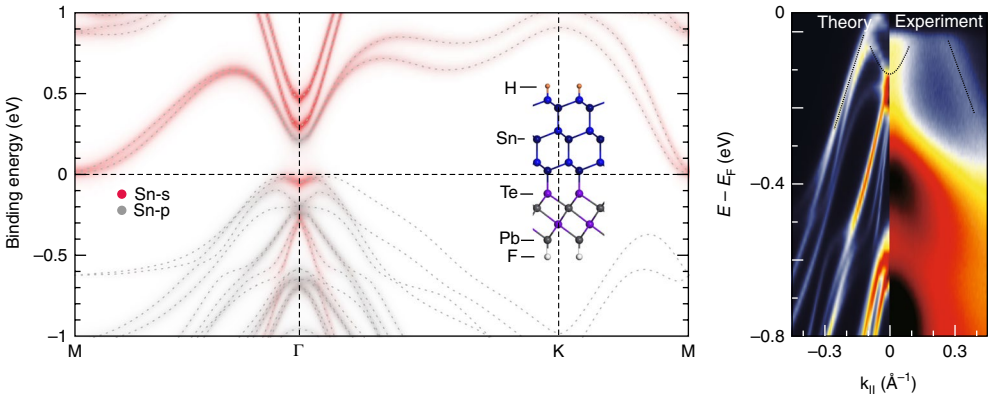

Fig. 4 | Calculated band structure of a trilayer stanene on PbTe. The inset illustrates the atomic model considered in the first-principles calculation. A hydrogenated trilayer stanene is placed on top of the PbTe substrate, which is simulated by a slab of two PbTe layers saturated by fluorine on the bottom. Red (grey) colour highlights the contributions from Sn s (p) orbitals, obtained by projecting the Bloch wavefunction onto the corresponding orbitals. This indicates an s–p band inversion at the Γ point. The right-hand panel compares the calculated bands with the ARPES data from 3-Sn/15-PbTe.

which agrees with our transport result by fitting the upper critical field data (Fig. 2b). In comparison, for the bulk β-Sn $\lambda \sim 0.7$ (ref. [11]).

We also performed first-principles calculations for a trilayer stanene grown on PbTe (see Methods). The calculated band structure, displayed in Fig. 4, looks somewhat complicated, since orbitals of stanene and PbTe hybridize strongly with each other, showing significant Rashba splitting. Nevertheless, there exist two series of valence bands mainly contributed by stanene located about 0–0.6 eV below the valence band maximum. Importantly, the top valence bands are "M" shaped, which could introduce an "electron pocket" centred at Γ if E_F is placed slightly below the valence band maximum. These features echo the ARPES data. Furthermore, orbital analysis shows that Sn s (p) orbitals make a significant contribution to the lowest conduction (highest valence) band, except at Γ, where an s–p band inversion happens. This band inversion results in a topologically non-trivial phase[16,20,35]. The trilayer stanene grown on PbTe is therefore a 2D topological insulator with $Z_2 = 1$ in theory (see Extended Data Figure 5). We note that a band inversion may be induced in $Pb_{1-x}Sn_xTe$ alloy by increasing Sn, which is accompanied by reopening of the bulk band gap[24,36,37]. Experimentally, we observed no bulk band gap closing in PbTe with the low-temperature deposition of Sn[19], ruling out a possible topological transition in the PbTe substrate.

The delicate dependence of T_c on N_{Sn} can be employed for an in-plane integration of topological insulator and superconductor in the same material with tunable properties. Another direction for future endeavour is to investigate the proximity effect in the vertical direction. Our sandwich structure allows atomically sharp interfaces between a superconductor, a tunable barrier and a topological insulator—Bi_2Te_3. The Fermi momentum of few-layer stanene is comparable to that of Bi_2Te_3. Furthermore, the superconducting thickness we estimated can be larger than the total thickness of Sn and PbTe layers (Extended Data Figure 3d), such that Cooper pairs may travel into Bi_2Te_3. In addition, stanene is robust against air exposure and can protect the more sensitive Bi_2Te_3. In general, the observation of superconductivity in few-layer stanene enriches the material pool for constructing topological devices.

Methods

Methods, including statements of data availability and any associated accession codes and references, are available at https://doi.org/10.1038/s41567-017-0031-6.

Received: 19 July 2017; Accepted: 4 December 2017;
Published online: 15 January 2018

References

1. Saito, Y., Nojima, T. & Iwasa, Y. Highly crystalline 2D superconductors. *Nat. Rev. Mater.* **2**, 16094 (2017).
2. Brun, C., Cren, T. & Roditchev, D. Review of 2D superconductivity: the ultimate case of epitaxial monolayers. *Supercond. Sci. Technol.* **30**, 013003 (2017).
3. Xing, Y. et al. Quantum Griffiths singularity of superconductor–metal transition in Ga thin films. *Science* **350**, 542–545 (2015).
4. Saito, Y., Kasahara, Y., Ye, J., Iwasa, Y. & Nojima, T. Metallic ground state in an ion gated two-dimensional superconductor. *Science* **350**, 409–413 (2015).
5. Tsen, A. W. et al. Nature of the quantum metal in a two-dimensional crystalline superconductor. *Nat. Phys.* **12**, 208–212 (2016).
6. Lu, J. M. et al. Evidence for two-dimensional Ising superconductivity in gated MoS_2. *Science* **350**, 1353–1357 (2015).
7. Xi, X. et al. Ising pairing in superconducting $NbSe_2$ atomic layers. *Nat. Phys.* **12**, 139–143 (2016).
8. Qin, S., Kim, J., Niu, Q. & Shih, C.-K. Superconductivity at the two-dimensional limit. *Science* **324**, 1314–1317 (2009).
9. Zhang, T. et al. Superconductivity in one-atomic-layer metal films grown on Si(111). *Nat. Phys.* **6**, 104–108 (2010).
10. Meissner, W. & Ochsenfeld, R. Ein neuer Effekt bei Eintritt der Supraleitfähigkeit. *Naturwissenschaften* **21**, 787–788 (1933).
11. Chang, K. J. & Cohen, M. L. Electron–phonon interactions and superconductivity in Si, Ge, and Sn. *Phys. Rev. B* **34**, 4552–4557 (1986).
12. Wang, L. L. et al. Epitaxial growth and quantum well states study of Sn thin films on Sn induced Si(111)-$2\sqrt{3} \times 2\sqrt{3}$ R30° V. *Phys. Rev. B* **77**, 205410 (2008).
13. Molle, A. et al. Buckled two-dimensional Xene sheets. *Nat. Mater.* **16**, 163–169 (2017).
14. Xu, Y., Gan, Z. & Zhang, S.-C. Enhanced thermoelectric performance and anomalous Seebeck effects in topological insulators. *Phys. Rev. Lett.* **112**, 226801 (2014).
15. Wang, J., Xu, Y. & Zhang, S.-C. Two-dimensional time-reversal-invariant topological superconductivity in a doped quantum spin-Hall insulator. *Phys. Rev. B* **90**, 054503 (2014).
16. Xu, Y. et al. Large-gap quantum spin Hall insulators in tin films. *Phys. Rev. Lett.* **111**, 136804 (2013).
17. Wu, S.-C., Shan, G. & Yan, B. Prediction of near-room-temperature quantum anomalous Hall effect on honeycomb materials. *Phys. Rev. Lett.* **113**, 256401 (2014).
18. Zhu, F.-F. et al. Epitaxial growth of two-dimensional stanene. *Nat. Mater.* **14**, 1020–1025 (2015).
19. Y. Zang, et al. Realizing an epitaxial stanene with an insulating bandgap. Preprint at http://arXiv.org/abs/1711.07035.
20. Chou, B.-H. et al. Hydrogenated ultra-thin tin films predicted as two-dimensional topological insulators. *New J. Phys.* **16**, 115008 (2014).
21. Chang, W. et al. Hard gap in epitaxial semiconductor–superconductor nanowires. *Nat. Nanotechnol.* **10**, 232–236 (2015).
22. Van de Walle, C. G. Hydrogen as a cause of doping in zinc oxide. *Phys. Rev. Lett.* **85**, 1012–1015 (2000).
23. Chang, K. et al. Discovery of robust in-plane ferroelectricity in atomic-thick SnTe. *Science* **353**, 274–278 (2016).

24. Yan, C. et al. Experimental observation of Dirac-like surface states and topological phase transition in $Pb_{1-x}Sn_xTe(111)$ films. *Phys. Rev. Lett.* **112**, 186801 (2014).
25. Talantsev, E. F. et al. On the origin of critical temperature enhancement in atomically thin superconductors. *2D Mater.* **4**, 025072 (2017).
26. Gurevich, A. Limits of the upper critical field in dirty two-gap superconductors. *Physica C* **456**, 160–169 (2007).
27. Weng, Z. F. et al. Two-gap superconductivity in $LaNiGa_2$ with nonunitary triplet pairing and even parity gap symmetry. *Phys. Rev. Lett.* **117**, 027001 (2016).
28. Zehetmayer, M. A review of two-band superconductivity: materials and effects on the thermodynamic and reversible mixed-state properties. *Supercond. Sci. Technol.* **26**, 043001 (2013).
29. Civale, L. & Serquis, A. *MgB2 Superconducting Wires Ch. 1* (World Scientific, Singapore, 2016).
30. Barfuss, A. et al. Elemental topological insulator with tunable Fermi level: strained α-Sn on InSb(001). *Phys. Rev. Lett.* **111**, 157205 (2013).
31. Rojas-Sanchez, J.-C. et al. Spin to charge conversion at room temperature by spin pumping into a new type of topological insulator: α-Sn films. *Phys. Rev. Lett.* **116**, 096602 (2016).
32. Meevasana, W. et al. Creation and control of a two-dimensional electron liquid at the bare $SrTiO_3$ surface. *Nat. Mater.* **10**, 114–118 (2011).
33. Boschker, H., Richter, C., Fillis-Tsirakis, E., Schneider, C. W. & Mannhart, J. Electron–phonon coupling and the superconducting phase diagram of the $LaAlO_3$–$SrTiO_3$ interface. *Sci. Rep.* **5**, 12309 (2015).
34. Matetskiy, A. V. et al. Two-dimensional superconductor with a giant Rashba effect: one-atom-layer Tl–Pb compound on Si(111). *Phys. Rev. Lett.* **115**, 147003 (2015).
35. Xu, Y., Tang, P. & Zhang, S.-C. Large-gap quantum spin Hall states in decorated stanene grown on a substrate. *Phys. Rev. B* **92**, 081112(R) (2015).
36. Dimmock, J. O., Melngailis, I. & Strauss, A. J. Band structure and laser action in $Pb_xSn_{1-x}Te$. *Phys. Rev. Lett.* **16**, 1193–1196 (1966).
37. Arachchige, I. U. & Kanatzidis, M. G. Anomalous band gap evolution from band inversion in $Pb_{1-x}Sn_xTe$ nanocrystals. *Nano Lett.* **9**, 1583–1587 (2009).

Acknowledgements

We thank Hong Yao and Canli Song for useful discussions. This work is financially supported by the Ministry of Science and Technology of China (2017YFA0304600, 2017YFA0302902), the National Natural Science Foundation of China (grant no. 11604176) and the Beijing Advanced Innovation Center for Future Chip (ICFC). Y.X. acknowledges support from Tsinghua University Initiative Scientific Research Program and the National Thousand-Young-Talents Program. S.-C.Z. is supported by the US Department of Energy, Office of Basic Energy Sciences, Division of Materials Sciences and Engineering under contract no. DE-AC02-76SF00515.

Author contributions

M.L. and Y.Z. contributed equally to this work. D.Z., K.H. and Q.-K.X. conceived the project. Y.Z. grew the samples and carried out ARPES measurements with the assistance of Y.G., M.L. and D.Z. carried out the transport measurements with the assistance of K.Z., M.L., D.Z., H.L., X.-P.H. and Y.-Y.W. made the two-coil mutual inductance measurements. Z.G. and Y.X. carried out first-principles calculations. D.Z. and Y.X. analysed the data and wrote the paper with input from K.H., X.-C.M., S.-C.Z. and Q.-K.X. All authors discussed the results and commented on the manuscript.

Competing interests

The authors declare no competing financial interests.

Additional information

Supplementary information is available for this paper at https://doi.org/10.1038/s41567-017-0031-6.

Reprints and permissions information is available at www.nature.com/reprints.

Correspondence and requests for materials should be addressed to D.Z. or Y.X. or Q.-K.X.

Publisher's note: Springer Nature remains neutral with regard to jurisdictional claims in published maps and institutional affiliations.

Methods

Growth. We use molecular beam epitaxy to grow our heterostructures (Omicron, base pressure 1×10^{-10} mbar). To ensure lattice matching, five quintuple layers of Bi_2Te_3 were first grown on top of Si(111) substrates. This was followed by the layer-by-layer growth of PbTe. Finally, we deposited Sn at a substrate temperature of around 120 K. The sample is then annealed at temperatures up to 400 K to improve the film quality. The crystalline quality is monitored by in situ reflective high-energy electron diffraction and scanning tunnelling microscopy (see Extended Data Figure 6). A layer-by-layer growth is maintained from a monolayer up to the quintuple layer. Above five layers, the growth tends to form islands. The lattice constant of stanene expands as the number of PbTe layers increases, as revealed by reflective high-energy electron diffraction[19].

Transport. Samples grown on intrinsic Si(111) substrate were employed for low-temperature transport measurements in a closed-cycle system (Oxford Instruments TelatronPT) equipped with an He-3 insert (base temperature = 0.25 K). The temperature sensor was placed directly below the sample stage and positioned in an orientation with minimal magnetoresistances. Freshly cut indium cubes were cold pressed onto the sample as contacts. Standard lock-in techniques were employed to determine the sample resistance in a four-terminal configuration with a typical excitation current of 100 nA at 13 Hz.

To fit upper critical field as a function of temperature in the two-band regime, we employ the formula[26]

$$\ln\frac{T}{T_c} = -\frac{\left[U\left(\frac{eD_1\mu_0H_{c2}}{hT}\right)+U\left(\frac{eD_2\mu_0H_{c2}}{hT}\right)+\frac{\sqrt{(\lambda_{11}-\lambda_{22})^2+4\lambda_{12}^2}}{\lambda_{11}\lambda_{22}-\lambda_{12}^2}\right]}{2}+$$
$$\left[\frac{\left(U\left(\frac{eD_1\mu_0H_{c2}}{hT}\right)-U\left(\frac{eD_2\mu_0H_{c2}}{hT}\right)-\frac{\lambda_{11}-\lambda_{22}}{\lambda_{11}\lambda_{22}-\lambda_{12}^2}\right)^2}{4}+\frac{\lambda_{12}^2}{(\lambda_{11}\lambda_{22}-\lambda_{12}^2)^2}\right]^{\frac{1}{2}},$$

where $U(x)=\psi\left(\frac{1}{2}+x\right)-\psi\left(\frac{1}{2}\right)$, with ψ the digamma function. D_1 and D_2 reflect the diffusivities of the two bands. λ_{11}, λ_{22} and λ_{12} are intraband and interband electron–phonon coupling constants, respectively. We fit the data of 3-Sn/10-PbTe with D_1, D_2, λ_{11}, λ_{22} and λ_{12} as fitting parameters. We then use the extracted values of λ_{11}, λ_{22} and λ_{12} and fit the data of 3-Sn/12-PbTe with D_1 and D_2 as free parameters.

For the activated transport, we use $R_{\mathrm{sheet}}=R_0(\mu_0H)e^{-\frac{U_H}{T}}$ to fit the data. U_H represents the activation energy. In regime I, $R_0(\mu_0H)$ scales as $R_0e^{\frac{U_H}{T_c}}$, with R_0 being independent of μ_0H. Also, U_H scales linearly with $\ln(\mu_0H)$ such that $-\frac{dU_H}{d\ln\mu_0H}=\frac{\Phi_0^2d}{256\pi^3\Lambda^2}$ (ref. [38]). Here Φ_0 is the flux quantum and Λ the London penetration depth normal to the superconducting film.

ARPES. Samples grown on highly doped Si(111) substrates were transferred to the analysis chamber without breaking the ultrahigh vacuum. ARPES with a photon energy of 21.22 eV (He-I light) was carried out with a Scienta R4000 spectrometer. For a quantitative analysis, we first extract the momentum k at a series of binding energies by fitting the peaks in the corresponding momentum distribution curves with Lorentzian functions. The obtained data points $k(E)$ (white circles in Fig. 3a) are then linearly fitted (dashed lines) to extract dE/dk as well as k_F.

First-principles calculations. Density functional theory calculations were performed with the Vienna ab initio simulation package, using the projector-augmented-wave potential, the Perdew–Burke–Ernzerhof exchange–correlation functional and the plane-wave basis with an energy cut-off of 400 eV. The periodic slab approach was employed to model stanene grown on PbTe, using a vacuum layer of 12 Å and a $12\times12\times1$ Monkhorst–Pack k grid. A slab of two Pb–Te bilayers with a surface lattice constant of 4.568 Å (based on the experimental value of bulk) was used to simulate the substrate, in which the bottom Pb–Te bilayer was fixed during relaxation and the bottom Pb atoms were saturated by fluorine to remove the dangling bonds on the bottom. The spin–orbit coupling was included in the self-consistent calculations of electronic structure.

Data availability. The data that support the findings of this study are available from the authors upon reasonable request.

References

38. Ephron, D., Yazdani, A., Kapitulnik, A. & Beasley, M. R. Observation of quantum dissipation in the vortex state of a highly disordered superconducting thin film. *Phys. Rev. Lett.* **76**, 1529–1532 (1996).

REPORT

SUPERCONDUCTIVITY

Type-II Ising pairing in few-layer stanene

Joseph Falson[1]*, Yong Xu[2,3,4], Menghan Liao[2], Yunyi Zang[2], Kejing Zhu[2], Chong Wang[2], Zetao Zhang[2], Hongchao Liu[5], Wenhui Duan[2,4,6], Ke He[2,4,7], Haiwen Liu[8]†, Jurgen H. Smet[1]†, Ding Zhang[2,4,7]†, Qi-Kun Xue[2,4,7]

Spin-orbit coupling has proven indispensable in the realization of topological materials and, more recently, Ising pairing in two-dimensional superconductors. This pairing mechanism relies on inversion symmetry–breaking and sustains anomalously large in-plane polarizing magnetic fields whose upper limit is predicted to diverge at low temperatures. Here, we show that the recently discovered superconductor few-layer stanene, epitaxially strained gray tin (α-Sn), exhibits a distinct type of Ising pairing between carriers residing in bands with different orbital indices near the Γ-point. The bands are split as a result of spin-orbit locking without the participation of inversion symmetry–breaking. The in-plane upper critical field is strongly enhanced at ultralow temperature and reveals the predicted upturn.

The realization of superconducting materials that are resilient to strong external magnetic fields remains an important pursuit for both applied and fundamental research (*1*–*7*). One recent breakthrough has been the identification of "Ising pairing" in two-dimensional (2D) crystalline superconductors (*2*). This pairing mechanism can apparently boost the in-plane upper critical field, $B_{c2,//}$. For example, molybdenum disulfide (MoS_2) (*3*, *4*), populated with charge carriers through ionic liquid gating, exhibits a $B_{c2,//}$ exceeding 52 T at a temperature T equal to ~20% of the zero-field superconducting transition temperature $T_{c,0}$. In atomically thin niobium diselenide ($NbSe_2$), $B_{c2,//}$ was reported to be 31.5 T at 10% $T_{c,0}$ (*5*), even though an isotropic bulk superconductor with the same $T_{c,0}$ would only sustain a field of up to 5.6 T, as set by the Chandrasekhar-Clogston or Pauli limit (*8*, *9*): $B_p = 1.86T_{c,0}$. In amorphous superconducting films, spin-orbit scattering (Fig. 1A) (*10*) has been attributed a key role in enhancing $B_{c2,//}$. However, in high-mobility crystalline samples, spin-orbit scattering can be safely discarded as the origin of the enhancement because it would imply unphysically short scattering times (*3*–*5*).

Theory has therefore pointed to properties inherent to the band structure of these 2D materials to account for the anomalous robustness. As a result of broken inversion symmetry, opposing valleys in k-space host states of opposite spin orientation (Fig. 1C); strong spin-orbit coupling (SOC) induces substantial spin splitting between these valleys. Consequently, Cooper pairs formed from carriers in opposing valleys possess locked opposite spins and become resilient to an in-plane pair-breaking field. This physical framework inaugurated the search for ever increasing $B_{c2,//}$ almost exclusively in transition-metal dichalcogenides because their crystal structure may naturally break in-plane inversion symmetry. Single layers of tungsten disulfide (WS_2) and tantalum disulfide (TaS_2)—both hosting heavier elements than those in MoS_2 and $NbSe_2$—were recently shown to support an even larger enhancement of $B_{c2,//}$ (*6*, *7*).

One key theoretical prediction for Ising superconductivity remains to be verified experimentally: $B_{c2,//}$ is expected to diverge and deviate from the 2D Ginzburg-Landau (G-L) formula at low temperatures, even if a moderate amount of disorder is present (*11*–*13*). Such behavior is reminiscent of the Fulde-Ferrell-Larkin-Ovchinnikov (FFLO) state (Fig. 1B) (*14*–*19*), an epitome of robust pairing against spin-polarizing fields in clean superconductors. There, macroscopic coherence gets replaced by a spatially ordered phase in the presence of a partial spin polarization at low temperatures, $T < 0.5T_{c,0}$. The experimental observation of a rapidly increasing $B_{c2,//}$ at low temperature provides strong support to the existence of the FFLO state in organic superconductors (*19*). In Ising superconductors, however, it is the spin split band structure that imposes a similar renormalization to the G-L formula at $T \ll T_{c,0}$. Unfortunately, the relevant magnetic field regime in the phase diagram as $T \to 0$ is difficult to access for established Ising superconductors owing to technical limitations in the attainable magnetic fields.

We identified a divergence of $B_{c2,//}$ at low temperature and breakdown of the G-L formula in epitaxial thin films of α-Sn(111), also referred to as few-layer stanene (*20*, *21*). This material has recently emerged as a 2D superconductor (*21*). By cooling the sample down to as low as 2% of $T_{c,0}$, we observed an anomalous increase of $B_{c2,//}$ by 30% over the conventional behavior in a temperature window as narrow as 200 mK.

The atomic structure of trilayer stanene grown on PbTe substrates with low-temperature molecular beam epitaxy is illustrated in Fig. 2A (*20*). The 3D rendering of the band structure of the trilayer based on angle-resolved photoemission spectroscopy (ARPES) data as well as first-principles calculations (*21*) is

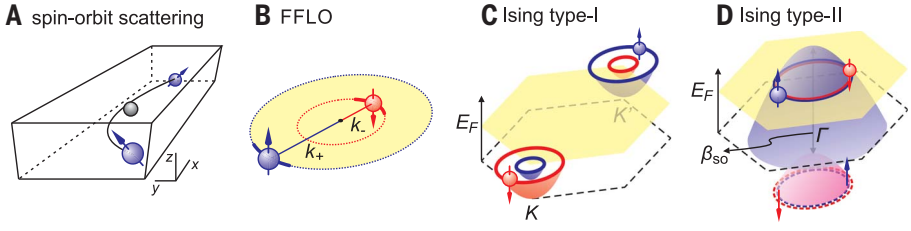

Fig. 1. Mechanisms for an enhanced in-plane upper critical field. (**A**) Spin-orbit scattering. Electronic spins get randomized through scattering off impurities. (**B**) FFLO state. Cooper pairs form with a finite momentum q. Only a small section of the Fermi surface can host pairs (solid curves). Owing to this finite momentum q, the order parameter is spatially modulated along the same direction, $\Delta = \Delta_0 e^{iqr}$. (**C**) Type-I Ising superconductivity, pairing of electrons in opposite spin split valleys. Only one pair of electron pockets centered on K and K' points are highlighted. (**D**) Type-II Ising superconductivity, pairing of charge carriers on orbits around the Γ-point with their spins aligned in the out-of-plane orientation. β_{SO} represents the SOC-induced splitting. Hole bands are illustrated as an example. Electron bands or bands with a more complicated dispersion are also allowed as long as the spin splitting is caused by the same SOC. The red and blue circles indicate two energetically degenerate bands with opposite spin orientations, each of which has a spin split counterpart below the Fermi level (indicated with the dashed circles).

[1]Max Planck Institute for Solid State Research, Stuttgart 70569, Germany. [2]State Key Laboratory of Low-Dimensional Quantum Physics, Department of Physics, Tsinghua University, Beijing 100084, China. [3]RIKEN Center for Emergent Matter Science (CEMS), Wako, Saitama 351-0198, Japan. [4]Frontier Science Center for Quantum Information, Beijing 100084, China. [5]International Center for Quantum Materials, Peking University, Beijing 100871, China. [6]Institute for Advanced Study, Tsinghua University, Beijing 100084, China. [7]Beijing Academy of Quantum Information Sciences, Beijing 100193, China. [8]Center for Advanced Quantum Studies, Department of Physics, Beijing Normal University, Beijing 100875, China.
*Present address: Department of Applied Physics and Materials Science, California Institute of Technology, Pasadena, CA, USA.
†Corresponding author. Email: haiwen.liu@bnu.edu.cn (H.L.); j.smet@fkf.mpg.de (J.H.S.); dingzhang@mail.tsinghua.edu.cn (D.Z.)

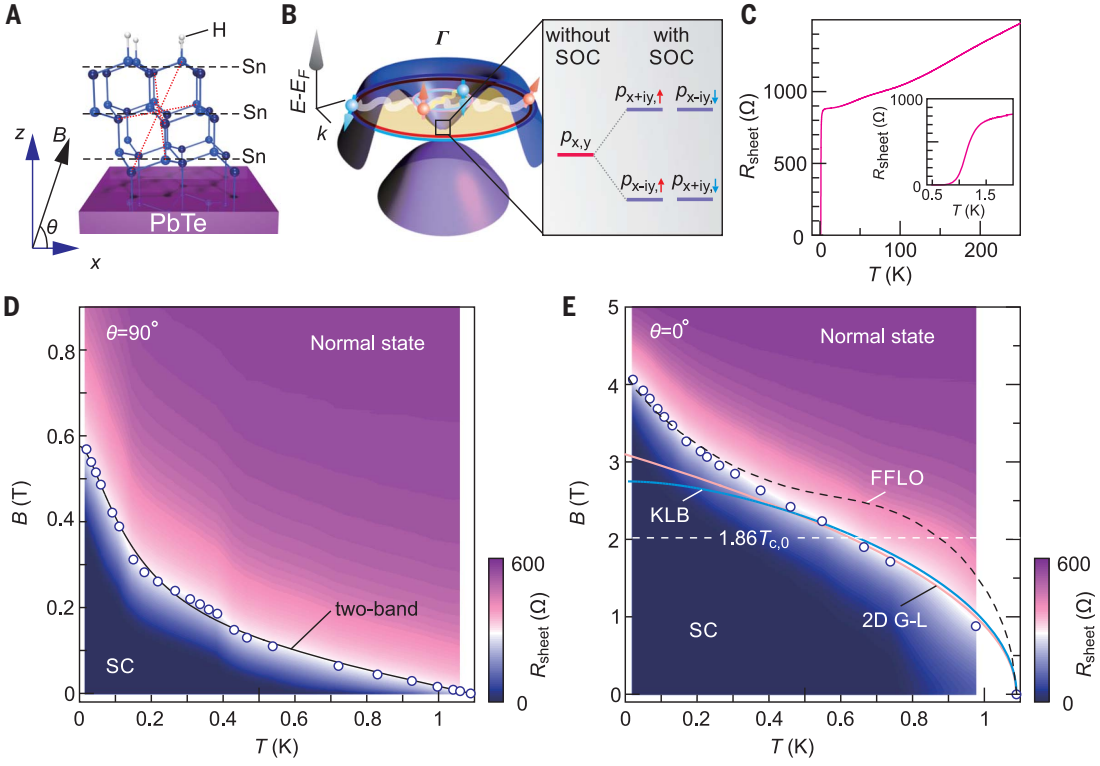

Fig. 2. Superconducting properties of trilayer stanene. (**A**) Atomic structure of hydrogen-decorated trilayer stanene on a PbTe substrate. Dashed lines indicate the three layers of Sn atoms. Red dotted lines indicate the inversion symmetry. (**B**) 3D schematic of the band structure of trilayer stanene. Blue and red circles reflect the hole-electron bands intersecting with the Fermi level. (Right) The band splitting around the Γ point owing to SOC. (**C**) Temperature-dependent sheet resistance of trilayer stanene grown on 12 layers of PbTe. (**D** and **E**) Color-coded resistance of the trilayer stanene on 12-PbTe as a function of (D) perpendicular and (E) in-plane magnetic field at a set of temperature points. The white stripe indicates the boundary between the superconducting (SC) and normal state. Circles represent the magnetic fields where the resistance becomes 50%R_n at a fixed T. Because of the smooth nature of this transition, determining B_{c2} by using another definition, such as 1%R_n or 10%R_n, would not change the general temperature-dependent behavior obtained. Solid and dashed curves are theoretical fits. The solid curve in (D) is based on the formula derived for a two-band superconductor (*23*). The blue curve in (E) was obtained by using the formula that takes into account the spin-orbit scattering as derived by Klemm, Luther, and Beasley (KLB) (*10*). The pink curve in (E) is based on the 2D G-L formula (*21*). The black dashed curve in (E) is based on the formula for a superconductor in the FFLO state (*16*). The white dashed line marks the Pauli limit using the standard Bardeen-Cooper-Schrieffer (BCS) ratio (*3*) as well as a *g*-factor of 2.

shown in Fig. 2B. In the vicinity of the Fermi level, a linearly dispersing hole band surrounds a small electron pocket at the Γ-point, giving rise to two-band superconductivity (*21*). We show in Fig. 2C the temperature dependence of the sheet resistance of a sample consisting of trilayer stanene that has been grown on a 12-layer-thick lead telluride (PbTe) buffer (3-Sn/12-PbTe) down to 250 mK (details of the sample preparation and measurement techniques are provided in the supplementary materials, materials and methods and supplementary text, note I); we observed a superconducting transition at the temperature of 1.1 K. Displayed in Fig. 2, D and E, are color renditions of the sample resistance in the parameter space spanned by the temperature and either the perpendicular (Fig. 2D) or the in-plane (Fig. 2E) magnetic field. They reflect the phase diagram of the superconducting ground state. The white color in Fig. 2, D and E, corresponds to approximately half of the normal state resistance (R_n) and hence demarcates the superconducting transition from the normal state; it also traces the temperature dependence of the upper critical magnetic fields indicated with open circles [setting the boundary at 1%R_n yields qualitatively the same results (figs. S3 to S7)]. Close to $T_{c,0}$, both $B_{c2,\perp}(T)$ and $B_{c2,//}(T)$ follow the 2D G-L formula (*21*), and deviations only become apparent at lower temperatures. The out-of-plane upper critical field $B_{c2,\perp}(T)$ exhibits an upturn, which is properly captured by the formula of a two-band superconductor (Fig. 2D, solid black curve) (*22*) that considers the orbital effect of the perpendicular magnetic field. However, when the magnetic field is applied parallel to an ultrathin superconductor, superconductivity is primarily suppressed by the paramagnetic effect, and the two-band formula reduces to a simple square root dependence on T (*22*), indistinguishable from that of the 2D G-L formula (Fig. 2E, pink curve). Clearly, such a two-band treatment fails to describe the enhancement in the in-plane upper critical field observed in experiment, which amounts to 1 T by cooling below T = 0.2 K. The in-plane upper critical field exceeds the Pauli limit by a factor of 2, assuming the common estimate of B_p = $1.86T_{c,0}$ for an isotropic bulk superconductor (we discuss the possible anisotropy in the supplementary text, note IV).

We next turned to elucidating the mechanism of the upper critical field enhancement in our samples. The upper critical fields of two trilayer stanene samples with differing PbTe buffer layer thicknesses are compared in Fig. 3A. The position of the Fermi level is known to decrease as the thickness of the buffer layer is decreased because of the reduced donation of carriers from PbTe (*21*). This results in a lower $T_{c,0}$ for trilayer stanene on six-layer PbTe. Nevertheless, this sample also exhibits a $B_{c2,//}(T)$ that clearly departs from that of the 2D G-L formula (fig. S4). It possesses a higher $B_{c2,//}/B_p$ at $T \rightarrow 0$ as compared with the 3-Sn/12-PbTe sample (Fig. 3A), although the divergence is less prominent. These results indicate that an unusual mechanism renders the Cooper pairs robust against in-plane fields. The spin-orbit scattering mechanism (*10*) can be readily ruled out because it disagrees with the experimental data (Fig. 2E, light blue curve marked "KLB"). The up-turn bears a striking resemblance to that observed in superconductors hosting the FFLO state. However, the mean free path (l) of our superconductor is ~10 nm (supplementary text, note II), which is much smaller than the coherence length ξ ~ 50 nm extracted from a linear fitting of $B_{c2,\perp}(T)$ close to $T_{c,0}$. We define $B_{c2,\perp}$ as the position at which the resistance drops to 50%R_n. Using the criterion of 1%R_n yields an even larger ξ (supplementary text, note II). By contrast, the FFLO state requires a clean superconductor with $l > \xi$ (*17*). Furthermore, the temperature dependence expected

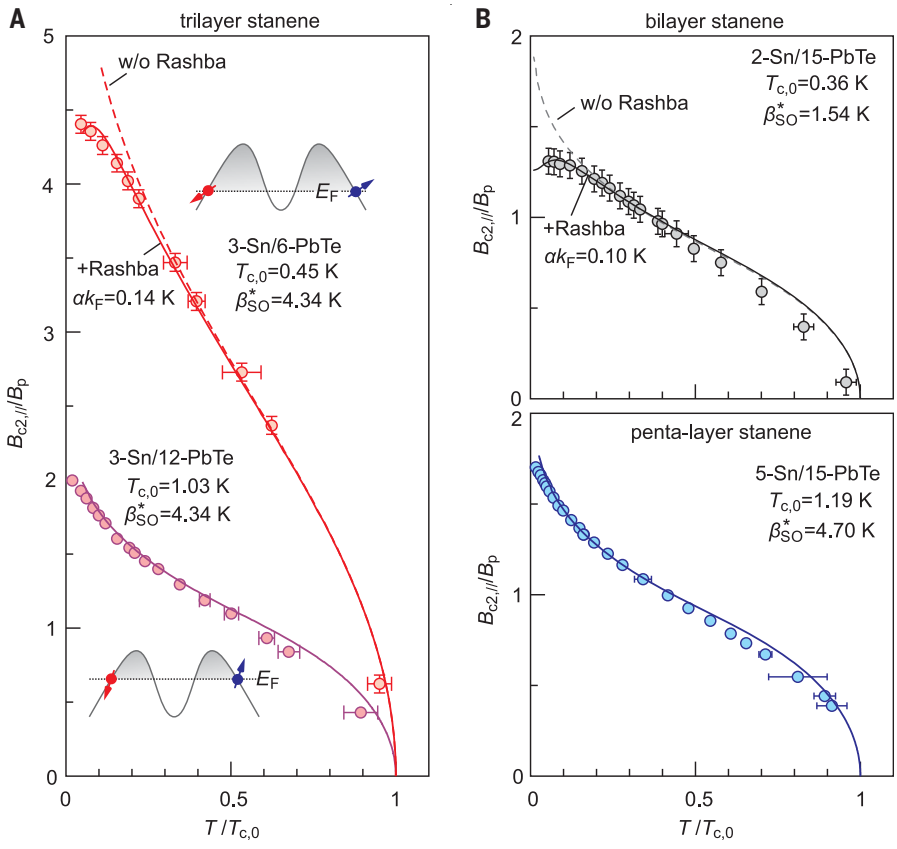

Fig. 3. Temperature dependence of the in-plane upper critical fields in few-layer stanene samples. (**A** and **B**) Data obtained from four samples with different stanene and PbTe substrate thicknesses. For example, 3-Sn/6-PbTe refers to a trilayer stanene grown on top of six layers of PbTe. The ratio of the in-plane upper critical fields—the magnetic fields at which the sample resistance becomes 50% of the normal state resistance at a given temperature—to the Pauli limit field $B_p = 1.86T_{c,0}$ are plotted as circular symbols. Vertical error bars arise from the step size of the magnetic field in obtaining the resistance data (fig. S2). Horizontal error bars stem from the temperature variation during each scan of the resistance data. Errors are smaller than the symbols for those data points without apparent error bars. Solid and dashed curves are theoretical fits by using the formula derived for a type-II Ising superconductor (supplementary text, note V). $T_{c,0}$ is the zero-field transition temperature. β^*_{SO} is the intrinsic SOC strength renormalized by disorder. αk_F denotes the renormalized Rashba SOC strength.

from a superconductor in the FFLO state (*16*) is different (Fig. 2E). Ising superconductivity also predicts an up-turn when temperature drops; however, few-layer stanene itself has no M_z mirror symmetry and is centrosymmetric in the free-standing case (*23*, *24*). The films under study have surface decoration and sit on a substrate (Fig. 2A), but this type of inversion symmetry–breaking induces only the Rashba effect, which is detrimental to Ising pairing. Moreover, stanene hosts bands around Γ-point, in contrast to MoS_2 or $NbSe_2$, whose spin-split bands are around K and K' points. Apart from these differences in atomic and electronic structure, the experimentally observed thickness dependence of $B_{c2,//}(T)$ also distinguishes few-layer stanene from the established Ising superconductors. Instead of a fast diminishing effect of Ising pairing in thicker films of transition-metal dichalcogenides (*7*), the up-turn stays prominent even in pentalayer stanene but is smeared out when the thickness is reduced down to a bilayer (Fig. 3B).

The distinct difference between stanene and the widely studied transition-metal dichalcogenides necessitates an alternative mechanism in stanene to produce the out-of-plane spin orientations. It should not rely on inversion symmetry–breaking and in addition be applicable for spin-degenerate Fermi pockets near time-reversal invariant momenta. We formulated our model by focusing on the bands that involve the p_x- and p_y-orbitals of Sn because they are the most relevant for electronic conduction according to previous ARPES results and first-principles calculations. The SOC lifts the fourfold degeneracy at the Γ-point (Fig. 2B) and results in two sets of spin-degenerate bands mainly composed of $(|+\uparrow\rangle, |-\downarrow\rangle)$ (Fig. 1D, solid circles) and $(|+\downarrow\rangle, |-\uparrow\rangle)$ (Fig. 1D, dashed circles), respectively, where + and − refer to the $p_x + ip_y$ and $p_x - ip_y$ orbitals, respectively (*23*). Thanks to spin-orbit locking (Fig. 1D), bands with different orbital indices experience an opposite out-of-plane effective Zeeman field. This Zeeman splitting is parametrized as $\beta_{SO}(k)$ and is strongly k-dependent. $\beta_{SO}(k)$ is extraordinarily large at the Γ-point, where a splitting of ~0.5 eV in monolayer stanene—equivalent to a field of ~10^3 T—can occur. However, it substantially weakens at larger k because of interorbital mixing, given that an in-plane magnetic field contributes a perturbation term to the Hamiltonian proportional to $\langle +\uparrow, -\downarrow|\sigma_x|+\uparrow, -\downarrow\rangle$, where σ_x is the Pauli matrix. This term is zero for $k = 0$ and exerts increasing influence at larger k. Even though $\beta_{SO}(k)$ decreases moderately with film thickness in few-layer stanene as a consequence of reduced band splitting in a quantum well setting, Ising-like pairing between $|+\uparrow\rangle$ and $|-\downarrow\rangle$ within the Fermi pockets near the Γ-point is expected to persist, and this pairing is anticipated to be robust against in-plane magnetic fields. Hence, we have termed this mechanism type-II Ising superconductivity in order to distinguish it from previous instances of Ising superconductivity.

A full theoretical derivation of the temperature dependence of $B_{c2,//}$ using the Gor'kov Green function is presented in the supplementary text, note V. We used the Bernevig-Hughes-Zhang Hamiltonian based on atomic orbitals of stanene (*23*) and took into account the spin-dependent scattering and Rashba effect. The solid and dashed curves in Fig. 3 are theoretical fits to the data by using the equations we derived from this model (eqs. S3 and S2, respectively). The temperature dependence is essentially governed by two fit parameters—the disorder renormalized SOC strength β^*_{SO} and the Rashba SOC strength αk_F—whereas the theoretically chosen $T_{c,0}$ is slightly adjusted within 5% of the experimental values to obtain the best fit (the values are listed in Fig. 3 and compared with experimental values in table S1). The model agrees well with experimental data and captures the prominent up-turn feature in the low-temperature regime. Within this framework, the physical origin of this up-turn can be traced back to the peculiar spin split bands associated with different orbitals (Fig. 1D), which are protected by the crystal structure. At T close to $T_{c,0}$, thermal activation results in a partial population of the upper two orbitals, suppressing the contribution of the spin-orbit–induced spin split effect on $B_{c2,//}$. Data in this regime therefore overlap with the 2D G-L formula. As T approaches zero, however, the charge carriers are polarized into the lower orbitals and cause the up-turn of $B_{c2,//}$. Quantitatively, the dimensionless parameter $\frac{\beta^*_{SO}}{T_{c,0}}$ controls the deviation point between the enhancement behavior characteristic for "Ising" superconductivity and

the behavior governed by the G-L formula. Typically, $\beta^*_{SO}/T_{c,0} \approx 4$ in our samples (3-Sn/12-PbTe, for example), and a clear up-turn appears at $T_c/T_{c,0} \approx 0.6$.

On the basis of the theoretical model, we can understand qualitatively the substrate- and layer thickness–dependence of $B_{c2,//}$. The smoothening in 3-Sn/6-PbTe in comparison with 3-Sn/12-PbTe can be attributed to the variation of the spin-locking strength as one moves away from the Γ-point along the inverted Mexican hat band shape (Fig. 3A, inset). Spins of the $|+\rangle$ and $|-\rangle$ orbitals are strongly locked out of plane at the Γ-point. This Ising-like orientation becomes, however, less favorable at larger momenta. Lowering the Fermi level therefore suppresses the spin polarization of the outer hole band, which can be simulated by an effective Rashba term in the Hamiltonian. The experimental data can be fitted well by taking into account this effect. The modified formula also nicely describes the upper critical fields of bilayer stanene (Fig. 3B). We attribute the missing up-turn feature to stronger inversion symmetry–breaking because the top Sn layer is decorated by hydrogen atoms, whereas the bottom Sn layer sits on the Te atoms of PbTe (we compare the band structures obtained from first-principles calculations in fig. S8). Following this line of reasoning, a pentalayer stanene should experience a weaker Rashba effect, giving rise to an apparent enhancement of $B_{c2,//}$ at low T (Fig. 3B, bottom). Our work points to a broader range of materials hosting such pairing mechanisms without the participation of inversion symmetry–breaking (*25*).

Note added in proof: After we submitted this report, similar observations were reported (*26*, *27*).

REFERENCES AND NOTES

1. A. Gurevich, *Nat. Mater.* **10**, 255–259 (2011).
2. Y. Saito, T. Nojima, Y. Iwasa, *Nat. Rev. Mater.* **2**, 16094 (2017).
3. J. M. Lu *et al.*, *Science* **350**, 1353–1357 (2015).
4. Y. Saito *et al.*, *Nat. Phys.* **12**, 144–149 (2015).
5. X. Xi *et al.*, *Nat. Phys.* **12**, 139–143 (2016).
6. J. Lu *et al.*, *Proc. Natl. Acad. Sci. U.S.A.* **115**, 3551–3556 (2018).
7. S. C. de la Barrera *et al.*, *Nat. Commun.* **9**, 1427 (2018).
8. A. M. Clogston, *Phys. Rev. Lett.* **9**, 266–267 (1962).
9. B. S. Chandrasekhar, *Appl. Phys. Lett.* **1**, 7–8 (1962).
10. R. A. Klemm, A. Luther, M. R. Beasley, *Phys. Rev. B* **12**, 877–891 (1975).
11. S. Ilić, J. S. Meyer, M. Houzet, *Phys. Rev. Lett.* **119**, 117001 (2017).
12. Y. Liu *et al.*, *Phys. Rev. X* **8**, 021002 (2018).
13. R. Wakatsuki, K. T. Law, Proximity effect and Ising superconductivity in superconductor/transition metal dichalcogenide heterostructures. arXiv:1604.04898 [cond-mat.supr-con] (2016).
14. P. Fulde, R. A. Ferrell, *Phys. Rev.* **135** (3A), A550–A563 (1964).
15. A. I. Larkin, Yu. N. Ovchinnikov, *Sov. Phys. JETP* **20**, 762 (1965).
16. H. Shimahara, *Phys. Rev. B Condens. Matter* **50**, 12760–12765 (1994).
17. Y. Matsuda, H. Shimahara, *J. Phys. Soc. Jpn.* **76**, 051005 (2007).
18. G. Zwicknagl, S. Jahns, P. Fulde, *J. Phys. Soc. Jpn.* **86**, 083701 (2017).
19. J. Wosnitza, *Ann. Phys.* **530**, 1700282 (2018).
20. Y. Zang *et al.*, *Adv. Funct. Mater.* **28**, 1802723 (2018).
21. M. Liao *et al.*, *Nat. Phys.* **14**, 344–348 (2018).
22. A. Gurevich, *Physica C* **456**, 160–169 (2007).
23. Y. Xu *et al.*, *Phys. Rev. Lett.* **111**, 136804 (2013).
24. Y. Xu, Z. Gan, S.-C. Zhang, *Phys. Rev. Lett.* **112**, 226801 (2014).
25. C. Wang *et al.*, *Phys. Rev. Lett.* **123**, 126402 (2019).
26. Y. Liu *et al.*, arXiv:1904.12719 [cond-mat.supr-con] (2019).
27. A. Devarakonda *et al.*, arXiv:1906.02065 [cond-mat.supr-con] (2019).
28. D. Zhang, Data for "Type-II Ising superconductivity in few-layer stanene". Harvard Dataverse (2020);

ACKNOWLEDGMENTS

We thank B. Friess for technical assistance and Y. Zhang for fruitful discussions. **Funding:** This work is financially supported by the National Natural Science Foundation of China (grants 11790311, 11922409, 11674028, and 51788104); the Ministry of Science and Technology of China (2017YFA0304600, 2017YFA0302902, 2017YFA0303301, 2018YFA0307100, 2018YFA0305603, and 2016YFA0301001); and the Beijing Advanced Innovation Center for Future Chip (ICFC). **Author contributions:** D.Z. conceived the project. J.F., D.Z., and M.L. performed the low-temperature electrical measurements. Y.Z., K.Z., and K.H. grew the samples. Y.X., C.W., Z.Z., and W.D. carried out first-principles calculations and theoretical analysis. Ha.L. derived the microscopic model of superconductivity with Ho.L.'s assistance. D.Z., J.F., Y.X., Ha.L., and J.H.S. analyzed the data and wrote the paper with input from Q.-K.X. All authors discussed the results and commented on the manuscript. **Competing interests:** The authors declare no competing interests; **Data and materials availability:** All data are available in (*26*).

SUPPLEMENTARY MATERIALS

science.sciencemag.org/content/367/6485/1454/suppl/DC1
Materials and Methods
Supplementary Text
Figs. S1 to S8
Table S1
References (*29*–*42*)

19 March 2019; accepted 27 February 2020
Published online 12 March 2020
10.1126/science.aax3873

Type-II Ising pairing in few-layer stanene

Joseph Falson, Yong Xu, Menghan Liao, Yunyi Zang, Kejing Zhu, Chong Wang, Zetao Zhang, Hongchao Liu, Wenhui Duan, Ke He, Haiwen Liu, Jurgen H. Smet, Ding Zhang and Qi-Kun Xue

Science **367** (6485), 1454-1457.
DOI: 10.1126/science.aax3873originally published online March 12, 2020

A resilient superconductor

Superconductivity typically does not fare well in the presence of magnetic fields, which tend to break the electron pairs that make a material superconducting. However, some materials, such as the recently discovered Ising superconductors, retain their properties in very high magnetic fields. Ising pairing was identified in transition metal dichalcogenides such as molybdenum disulfide and required the breaking of inversion symmetry. Falson *et al.* have now found a similar resilience to in-plane magnetic fields in another two-dimensional material, few-layer stanene. The band structure of stanene and the lack of inversion symmetry breaking in the system required a distinct theoretical model to explain this property, now dubbed type II Ising pairing.

Science, this issue p. 1454